

# The performance of a cryogenically cooled monochromator for an in-vacuum undulator beamline

Lin Zhang,<sup>a\*</sup> Wah-Keat Lee,<sup>a,b</sup> Michael Wulff<sup>a</sup> and Laurent Eybert<sup>a</sup>

<sup>a</sup>European Synchrotron Radiation Facility, BP 220, F-38043 Grenoble CEDEX, France, and <sup>b</sup>Advanced Photon Source, Argonne National Laboratory, 9700 South Cass Avenue, Argonne, IL 60439, USA. E-mail: zhang@esrf.fr

The channel-cut silicon monochromator on beamline ID09 at the European Synchrotron Radiation Facility is indirectly cooled from the sides by liquid nitrogen. The thermal slope error of the diffracting surface is calculated by finite-element analysis and the results are compared with experiments. The slope error is studied as a function of cooling coefficients, beam size, position of the footprint and power distribution. It is found that the slope error *versus* power curve can be divided into three regions: (i) The linear region: the thermal slope error is linearly proportional to the power. (ii) The transition region: the temperature of the Si crystal is close to 125 K; the thermal slope error is below the straight line extrapolated from the linear curve described above. (iii) The non-linear region: the temperature of the Si crystal is higher than 125 K and the thermal slope error increases much faster than the power. Heat-load tests were also performed and the measured rocking-curve widths are compared with those calculated by finite-element modeling. When the broadening from the intrinsic rocking-curve width and mounting strain are included, the calculated rocking-curve width *versus* heat load is in excellent agreement with experiment.

**Keywords:** X-ray optics; silicon-crystal monochromators; thermal deformation; cryogenic cooling; finite-element modeling.

## 1. Introduction

The brightest X-ray beams at the European Synchrotron Radiation Facility (ESRF) are produced by in-vacuum undulators, which have their magnets inside the vacuum vessel of the storage ring. These undulators emit 350–650 W of power in the central cone and the power density, at the position of the X-ray optics 30 m from the source, is between 70 and 170 W mm<sup>-2</sup>. Present plans at the ESRF and the Advanced Photon Source (APS) to increase the storage-ring current could increase these levels by 50–200%. This increasing heat load is an on-going challenge for the design of beamline optics, especially for crystal monochromators with relatively high incidence angles. The aim of this paper is to determine a theoretical and practical power limit for liquid-nitrogen-cooled silicon monochromators.

Liquid-nitrogen-cooled silicon crystals have been used with great success at high heat loads (Marot *et al.*, 1992; Rogers *et al.*, 1995; Lee *et al.*, 1995; Marot, 1995; also see the review by Bilderback *et al.* 2000). The thermal deformation of the crystal induced by heat load depends on the ratio  $\alpha/k$ , where  $\alpha$  and  $k$  are the thermal expansion coefficient and the thermal conductivity of the crystal, respectively. This ratio is strongly temperature dependent for silicon (Fig. 1). The value of the ratio  $\alpha/k$  is zero at 125 K, and about 50 times smaller at liquid-nitrogen temperature (77 K) than at room temperature. The performance limits of a cryogenically cooled silicon monochromator have

been studied theoretically by Zhang (1993) by finite-element analysis (FEA) and experimentally by Lee *et al.* (2000, 2001). Moreover, Tajiri *et al.* (2001) improved the FEA analysis by introducing the volume absorption effect.

FEA simulations can determine the strain field in a heat-distorted crystal. Most heat-load experiments, however, measure the rocking-curve widths. In order to compare FEA predictions with experiments, it is necessary to solve the Takagi–Taupin equations (Takagi, 1962, 1969; Taupin, 1964, 1967) including the FEA strain field. This approach has been successfully applied to water-cooled and liquid-nitrogen-cooled monochromators (Zhang *et al.*, 2001; Mocella *et al.*, 2001, 2003; Hoszowska *et al.*, 2001). These studies clearly show that for large distortions it is necessary to solve the Takagi–Taupin equations. For small distortions on the other hand, a simple geometrical approach is sufficient. In this simple approach the crystal is assumed to behave as a mirror with a narrow angular acceptance. In this paper we present results of FEA simulations and experimental measurements on the indirectly liquid-nitrogen-cooled channel-cut silicon monochromator on beamline ID09 at the ESRF. Since the measured thermal distortion is relatively small, we shall use the simple geometrical approach in the comparison between the FEA simulations and the experiments.

## 2. Experimental details

Beamline ID09 at the ESRF is a dual-purpose beamline for time-resolved and high-pressure experiments. The beamline was recently upgraded to include an in-vacuum undulator (U17), a cryogenically cooled monochromator and a high-precision toroidal mirror. The intensity and stability of the beam are critically important for time-resolved experiments. With the design of the low- $K$  in-vacuum undulator U17, we have attempted to strike a good compromise between brilliance and low heat load (Schotte *et al.*, 2002). The U17 undulator has a  $K$  value of 0.835 at a 6.0 mm gap. Its spectrum is dominated by the first harmonic so much so that one could call the undulator a single-harmonic undulator. The fundamental energy is 15.0 keV and polychromatic power in the central cone is 350 W at a current of 200 mA.

The experiments were performed on beamline ID09 on two different occasions under slightly different conditions. The first set of measurements were performed using the second undulator in the beamline, U46, at its minimum gap of 15.8 mm. The heat load on the crystal was varied by changing the beam size on the crystal. Later, the U17 undulator was installed, which increased the available beam power. The second set of measurements were carried out with the undulators in tandem. The beam size was fixed, but the incident

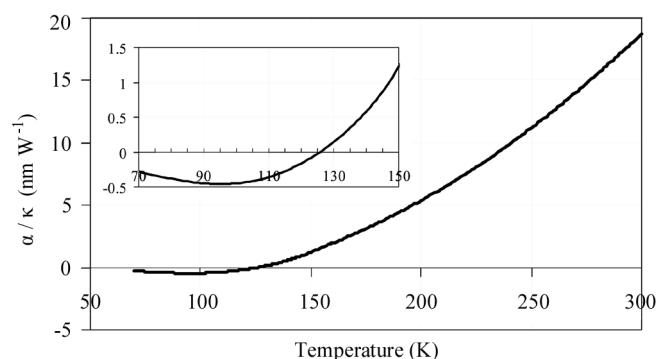


**Figure 1** Ratio of the thermal expansion coefficient and the thermal conductivity  $\alpha/k$  of silicon *versus* temperature.

power was varied by changing the U17 gap. In this case the in-vacuum undulator was used as a variable heat source. The monochromator, which is placed 31.39 m from the source point, was rotated to a Bragg angle of 14.3° which produced a 8.0 keV beam from Si(111). The rocking curves were determined by rotating the second reflecting surface about a weak link between the two surfaces. A silicon PIN diode with a 2.0 mm aluminium filter in front of it was used to detect higher-order high-energy photons. The detected photons dominated the 24 keV photons from Si(333) and the 32 keV photons from Si(444). Using U17 as a source of variable additional power has the advantage that, since it is a single-line undulator with the fundamental around 15 keV, a gap change does not significantly alter the intensity or spatial distribution of the 24 or 32 keV photons, which are mainly produced by the U46 undulator. Table 1 summarizes the parameters for the two experiments.

The maximum size of the incoming beam, measured in the plane normal to the direction of the beam, is 10.35 mm in the horizontal (H) direction and 2.3 mm in the vertical (V) direction. This beam size was defined by opening the primary slits, located 27.3 mm from the source point, to a horizontal gap  $H_{\text{slit}}$  of 9 mm and a vertical gap  $V_{\text{slit}}$  of 2 mm. The (projected) footprint on the Si crystal is  $H \times V / \sin \theta_{\text{Bragg}} = 10.35 \text{ mm} \times 9.31 \text{ mm}$ .

Calorimetric measurements were carried out to check the powers calculated using the *SRW* code (Chubar & Elleaume, 1998) or the *XOP* code (Dejus & Del Rio, 1996) and to check for absorption losses in the front end. When the *K*-parameter of the insertion device (*i.e.* the magnetic field) is fine-adjusted to agree with the measured fundamental energy of the undulators, the calorimetric measurements were in agreement with *SRW* and *XOP* to within 2%. The power values quoted in this paper are therefore those calculated by *SRW* or *XOP*.

### 3. FEA description

In this section we describe the power distribution of the beam, the cooling parameters and the finite-element model of the channel-cut crystal.

#### 3.1. Power absorption

The power density of the incident beam onto the crystal surface was calculated in the horizontal *x*-direction and in the vertical *y*-direction using the *SRW* and *XOP* codes. Gaussian fits were made in both directions. The normal-incidence power density distribution is then given by

$$Pa(x, y) = Pa_0 \exp(-x^2/2\sigma_x^2) \exp(-y^2/2\sigma_y^2), \quad (1)$$

with a peak power density  $Pa_0$ , and standard deviations  $\sigma_x = 8.114 \text{ mm}$ ,  $\sigma_y = 1.448 \text{ mm}$  (for undulator U46, gap 16.9 mm) at the position of the monochromator in normal incidence. The relationship between the total absorbed power  $P$  and the peak power density is

$$P = \int Pa(x, y) dx dy = f_{\text{bmsz}} 2\pi\sigma_x\sigma_y Pa_0, \quad (2)$$

where  $f_{\text{bmsz}}$  is an integral factor that depends on the beam size. This factor is  $f_{\text{bmsz}} = 1$  for the full beam, and  $f_{\text{bmsz}} = 0.276$  for a beam size of 10.35 mm (H)  $\times$  2.3 mm (V). The Gaussian distribution given in equation (1) leads to a difference of about 4% between the integrated power in equation (2) and the *SRW* computed power. In the FEA the peak power density is determined by the total absorbed power from equation (2). For example, for a total power  $P$  of 200 W the peak power density on the crystal surface  $Pa_0$  is  $11.2 \text{ W mm}^{-2}$  for a beam

**Table 1**  
Measurement parameters.

	First measurement	Second measurement
Undulators	U46	U46 and U17
Beam size (H $\times$ V)†	Varied	10.35 mm $\times$ 2.3 mm
Filter/window	0.5 mm C + 0.5 mm Be	0.4 mm diamond
Crystal Bragg angle	14.3°	14.3°

† Normal incidence at the crystal position.

size 10.35 mm (H)  $\times$  2.3 mm (V) at the position of the monochromator at normal incidence.

To account for the in-depth volume absorption of the X-ray beam, the Si crystal was divided into layers, each of thickness  $\Delta t = 0.5 \text{ mm}$ . The absorbed power in each layer was computed from the integration of the product of the spectral flux of the incoming beam at that depth and the spectral absorption of Si. The absorption factor  $f_{\text{vabs}}$  is defined as the ratio of the absorbed power in a given depth to the incident power on the crystal surface. This power absorption factor is shown in Fig. 2. The power absorption factors  $f_{\text{vabs}}$  in the two cases are almost identical. Note that the first and second layers absorb 39–42% and 13–14% of the total power, respectively.

When the Gaussian beam distribution and the volume absorption are considered, the power absorbed by a unit volume is given by

$$\frac{dP}{dV} = \frac{Pa(x, y)}{\Delta t} f_{\text{vabs}}. \quad (3)$$

Combining (1) and (3) we obtain

$$\frac{dP}{dV} = \frac{f_{\text{vabs}} Pa_0}{\Delta t} \exp(-x^2/2\sigma_x^2) \exp(-y^2/2\sigma_y^2). \quad (4)$$

The following four cases were studied by FEA to elucidate the importance of the different power distributions:

- (i) Gaussian distribution and volume absorption – most complete, as defined by equation (4);
- (ii) Gaussian distribution and surface absorption – as defined by equation (1);
- (iii) Uniform distribution and volume absorption;
- (iv) Uniform distribution and surface absorption.

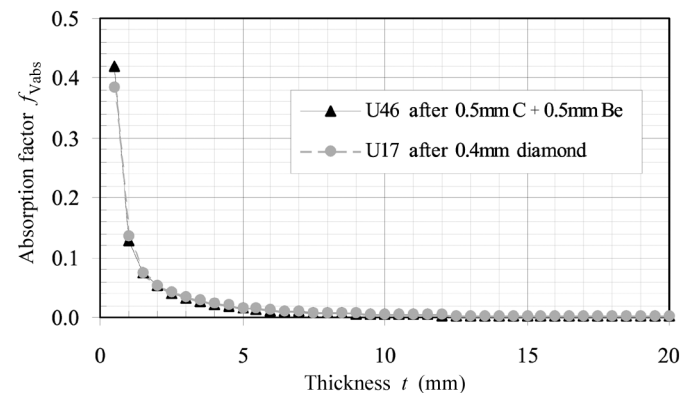


**Figure 2**  
Power absorption factor as a function of depth in the Si crystal. The spectrum of the U46 undulator is calculated at 16 mm gap and that of U17 at 6 mm gap. The Bragg angle is 14.3° and the beam size 10.35 mm (H)  $\times$  2.3 mm (V).

### 3.2. Cooling coefficient

The channel-cut crystal is indirectly cooled from both sides of the first diffracting surface. The cooling interface consists of an indium foil which is ‘sandwiched’ between the crystal and liquid-nitrogen-cooled Cu absorbers. For liquid nitrogen flow in a circular tube, the best possible value of the cooling coefficient is about  $h_{cv0} = 10000 \text{ W m}^{-2} \text{ K}^{-1}$ . The interface Cu–In–Si introduces a thermal contact resistance  $R_c \simeq 10^{-4} \text{ m}^2 \text{ K W}^{-1}$  (Marot & Rossat, 1992). Finally, the effective cooling coefficient  $h_{cv}$  on the crystal sides can be calculated as (Zhang, 1993)

$$h_{cv} = \left[ \frac{1}{f_a h_{cv0}} + R_c + R(\text{Cu}) + R(\text{In}) \right]^{-1}, \quad (5)$$

where  $f_a$  is the ratio of the cooling channel surface area and the contact surface area,  $R(\text{Cu})$  and  $R(\text{In})$  are the thermal conduction resistances in the copper block and in the indium foil, respectively. The effective cooling coefficient on the crystal sides is about  $5000 \text{ W m}^{-2} \text{ K}^{-1}$ . The real cooling coefficient may differ from this value owing to the actual value of thermal contact resistance  $R_c$  which is quite sensitive to the quality of the surface contact and to the contact pressure (Chantrenne *et al.*, 2003). We have therefore investigated how sensitive the slope error is to the cooling coefficients  $h_{cv}$ . We have calculated the following cases:

- (i)  $h_{cv} = 3000 \text{ W m}^{-2} \text{ K}^{-1}$  – fair thermal contact between the copper and the silicon crystal;
- (ii)  $h_{cv} = 5000 \text{ W m}^{-2} \text{ K}^{-1}$  – good thermal contact;
- (iii)  $h_{cv} = 8000 \text{ W m}^{-2} \text{ K}^{-1}$  – excellent thermal contact;
- (iv)  $h_{cv} = 18000 \text{ W m}^{-2} \text{ K}^{-1}$  – side cooling coefficient equivalent to direct internal cooling system with a cooling coefficient of  $h_{cv0} = 10000 \text{ W m}^{-2} \text{ K}^{-1}$ .

### 3.3. Finite-element model (FEM)

Owing to the difficulty in describing the indium interface, the thermal deformation was calculated by FEA neglecting the mechanical interface to the cooling blocks as described by Zhang (1993). An effective cooling coefficient was applied to the side surfaces of the crystal in contact with the copper block. The FEM is based on a CAD file without any simplification. Fig. 3(a) shows the FEM of the channel-cut Si crystal with the beam footprint, assuming a Gaussian beam distribution and surface absorption, and Fig. 3(b) shows a magnified view of the heat loading in the case of volume absorption. Note that the heat load from the reflected monochromatic beam on the second crystal is negligible.

The beam size of  $10.35 \text{ mm} \times 2.3 \text{ mm}$  is smaller than two standard deviations ( $\sigma_x = 8.114 \text{ mm}$ ,  $\sigma_y = 1.448 \text{ mm}$ ). In the case of a Gaussian distribution, the power density varies by only about 20% from the center to the edge of the footprint. In the case of volume absorption, heat load was applied on the volume generated by a  $10.35 \text{ mm} \times 2.3 \text{ mm}$  rectangular surface projected along a line in the  $xy$  plane and inclined  $14.3^\circ$  to that surface [see Fig. 3(b)]. The length of the inclined volume is 15 mm. The 15 mm-thick silicon absorbs about 95% of the X-ray power from the U17 undulator at 6 mm gap or from the U46 undulator at 16 mm gap. The mesh was generated to have an inclined length of 0.5 mm. This modeling is a better description of volume absorption than the model of staggered layers used by Tajiri *et al.* (2001).

The thermal conductivity  $\kappa$  and the thermal expansion coefficient  $\alpha$  are temperature dependent as shown in Fig. 1. A Poisson ratio  $\nu = 0.28$  of silicon was used in the FEA. The calculations assume the crystal to be free of mechanical constraints from the absorbers.

## 4. FEA results

### 4.1. Thermal slope error versus power distribution

To study the effect of different power distributions the performance of the four heat-load distributions described in §3.1 were studied by FEA. A thermal slope error was computed from the vertical displacement on the crystal surface along the meridian axis along the footprint. The peak-to-valley thermal slope error under the footprint versus the absorbed power is shown in the four cases in Fig. 4(a). The FEA was carried out with a cooling coefficient of  $h_{cv} = 5000 \text{ W m}^{-2} \text{ K}^{-1}$ . The same results in thermal slope error are also plotted versus the maximum temperature on the crystal surface in Fig. 4(b). Note that the temperature of the crystal is not uniform. The maximum temperature on the crystal surface is calculated by FEA.

In general, one can divide the slope–power curves shown in Fig. 4(a) into three regions:

- (i) The linear region ( $P \leq 300 \text{ W}$ ): the thermal slope error is linearly proportional to the power. In this region the maximum temperature of the Si crystal is below 125 K.
- (ii) The transition region ( $300 < P \leq 550 \text{ W}$ ): the temperature of the Si crystal is around 125 K where the thermal expansion coefficient is zero. The thermal slope error is below the extrapolated value from the linear region. There is a minimum of thermal slope error in this region.
- (iii) The non-linear region ( $P > 550 \text{ W}$ ): the thermal slope error increases quickly with power and the temperature of the crystal is greater than 125 K.

The linear and non-linear regions were predicted in an earlier study by Zhang (1993). In that study the cooling coefficient was optimized and thus variable at a given power. The two regions were

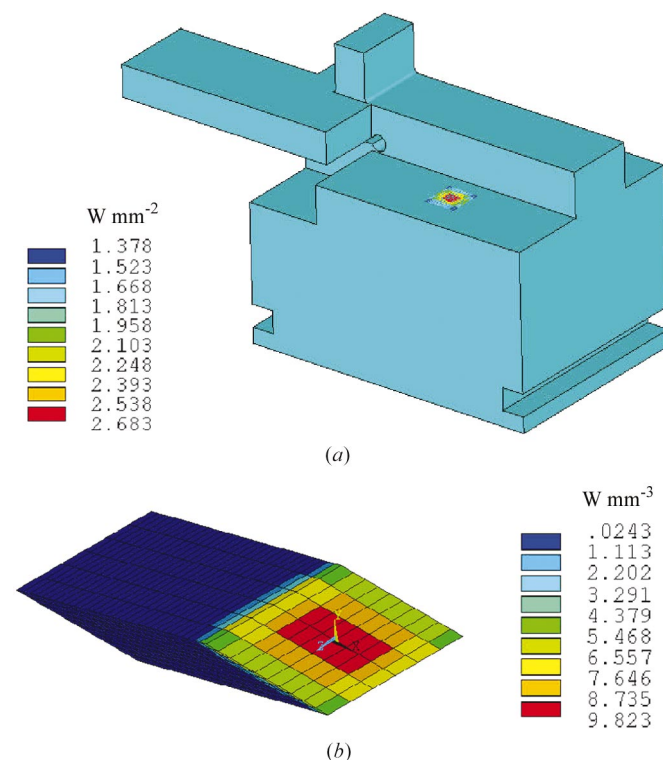


**Figure 3**  
(a) Finite-element model of the ESRF ID09 channel-cut Si crystal monochromator with a heat load with a Gaussian spatial distribution and surface absorption. (b) A magnified view of the heat loading for the volume absorption case. The scales of power densities correspond to a total absorbed power of 200 W.

characterized by their values of  $\theta_{th}/P$ ; the linear region is described by the relation  $\theta_{th}/P = \text{constant}$  and the non-linear region was approximated by  $\theta_{th}/P^{4.6} = \text{constant}$ .

The local minimum in the transition region in Fig. 4(a) was predicted by FEA during the design phase of this channel-cut Si crystal (Zhang, 1999). It was also observed by Lee *et al.* (2001) in an indirectly cryogenically cooled Si monochromator at the APS.

As the power density varies by only about 20% from the center to the edge of the footprint in the Gaussian distribution, the thermal slope errors are almost the same in the two cases: the slope error from a uniform distribution is 2.4% smaller than the slope error from a Gaussian distribution. If slits were opened to more than twice the value of  $\sigma_x$  and  $\sigma_y$ , the Gaussian power distribution would be needed.

The inclusion of the in-depth volume absorption effect reduces the thermal slope error by 18% as compared with surface absorption. This difference depends on the spectrum of the incident beam and the Bragg angle. In general, the volume absorption effect is essential for high-energy X-ray beams.

#### 4.2. Thermal slope error versus cooling coefficients

The thermal conductivity and the thermal expansion coefficient of silicon, as well as the ratio  $\alpha/\kappa$ , are temperature dependent, especially for temperature above 125 K (Fig. 1). The temperature of the crystal is therefore strongly dependent on the cooling coefficient  $h_{cv}$ , which is therefore an important parameter for the slope error. The FEA-calculated slope error is shown in Fig. 5(a) versus the power and in Fig. 5(b) versus the calculated peak temperature of the crystal for four values of the cooling coefficients ( $h_{cv} = 3000, 5000, 8000$  and  $18000 \text{ W m}^{-2} \text{ K}^{-1}$ ) as described in §3.2. The calculations were performed using Gaussian distributions and volume absorption.

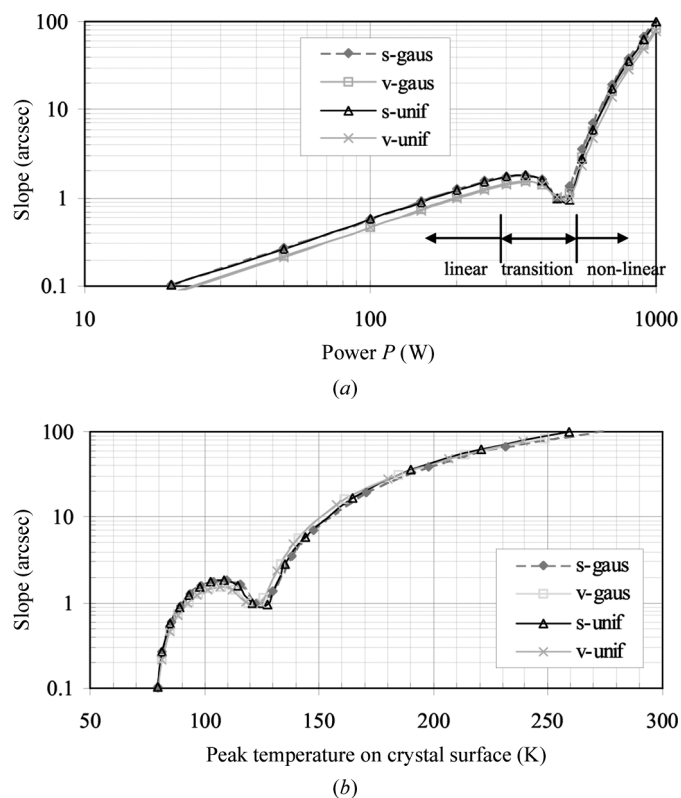


**Figure 4** Thermal slope error versus (a) absorbed power and (b) peak temperature on the crystal surface in the four heat-load cases: s: surface absorption; v: volume absorption; gaus: Gaussian distribution; unif: uniform distribution.

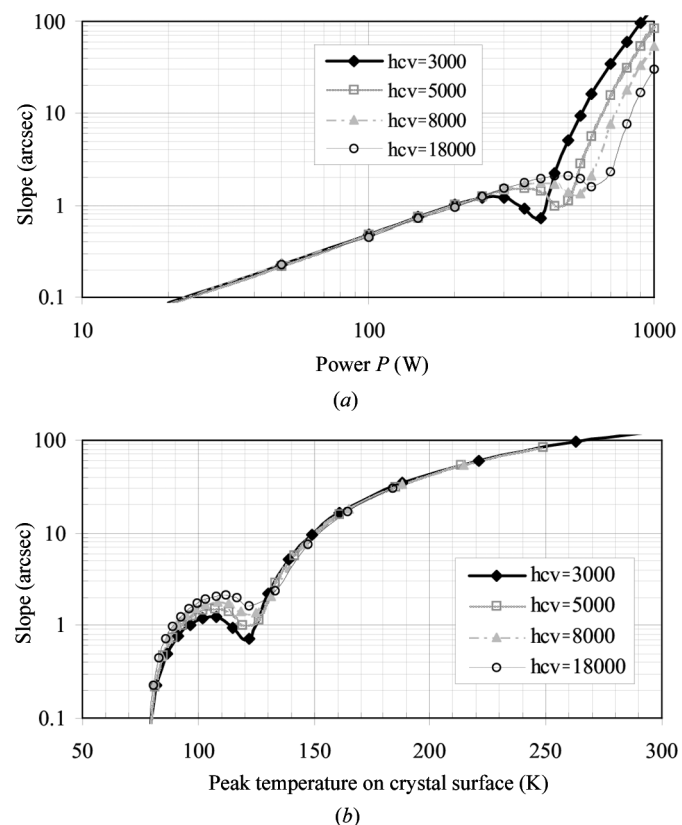
The calculations show that the thermal slope error is independent of the cooling coefficient  $h_{cv}$  in the linear region ( $P \leq 300 \text{ W}$ ) when  $h_{cv} \geq 3000 \text{ W m}^{-2} \text{ K}^{-1}$ . This can be explained by the fact that the curve of the ratio  $\alpha/\kappa$  versus temperature of the silicon crystal (Fig. 1) is quite flat for temperatures below 125 K. In the non-linear region ( $P > 300 \text{ W}$ ) the ratio  $\alpha/\kappa$  increases quickly with the temperature increase and the temperature depends on the cooling coefficient. Consequently the thermal slope error is strongly dependent on the cooling coefficient. For example, the slope error at 700 W is 2.4 arcsec at  $h_{cv} = 18000 \text{ W m}^{-2} \text{ K}^{-1}$  and 34 arcsec at  $h_{cv} = 3000 \text{ W m}^{-2} \text{ K}^{-1}$ . In addition, the linear region is wider for higher values of  $h_{cv}$ . For a comparison with direct cooling we also show the case of  $h_{cv} = 18000 \text{ W m}^{-2} \text{ K}^{-1}$ . The conclusion from Fig. 5(a) is that indirect cooling is sufficient for powers up to 450 W, but that direct cooling is necessary for powers above 450 W.

Fig. 5(b) shows that the thermal slope error versus the peak temperature ( $T_{\text{peak}}$ ) of the crystal is almost independent of the cooling coefficient, except in the transition region around  $T_{\text{peak}} = 125 \text{ K}$ .

#### 4.3. Thermal slope error versus beam size

By varying the opening of the slits we can vary the footprint and the heat load on the crystal. Figs. 6(a) and 6(b) show, respectively, the slope error versus power and versus the peak temperature of the crystal for five beam sizes (normal incidence):  $10 \text{ mm (H)} \times 2 \text{ mm (V)}$ ,  $10 \times 1, 5 \times 2, 2 \times 1$  and  $1 \times 1$ . The FEA was carried out with Gaussian distributions, surface absorption and a cooling coefficient  $h_{cv} = 5000 \text{ W m}^{-2} \text{ K}^{-1}$ .

The slope–power curves vary tremendously with beam size since the temperature distribution in the crystal varies tremendously with



**Figure 5** Thermal slope error versus (a) absorbed power and (b) peak temperature on the crystal surface for four different cooling coefficients.

the beam size or power distribution. At constant power the power density is smaller when the beam is bigger. The surface area of a 10 mm × 2 mm beam is twice that of a 10 × 1 or a 5 × 2 beam, but the power density of a 10 × 2 beam is 1/1.92 times that at 10 × 1 or 5 × 2. The thermal slope error at 10 × 2 is smaller than at 10 × 1 or 5 × 2, especially in the non-linear region. In other words, the thermal slope error at a given total power is significantly smaller when the beam size is larger (the power density is smaller). For example, the beam size 10 mm (H) × 2 mm (V) is 20 times bigger than 1 mm (H) × 1 mm (V), and the power density is 18 times smaller. However, the thermal slope error at  $P = 350$  W (non-linear region) is about 50 times smaller, and four times smaller in the linear region ( $P < 100$  W). The influence of the beam size or footprint is linked to the power density.

Elsewhere in this study, the beam size is assumed to be 10.35 mm (H) × 2.3 mm (V) unless explicitly stated.

Results in Fig. 6(b) show that the thermal slope error *versus* peak temperature of the crystal also varies with the beam size. The quite similar shape of the slope–temperature curves in Figs. 4(b), 5(b) and 6(b) comes from the absolute value of  $\alpha(T - T_f)$ ; here  $T_f = 77$  K is the temperature of liquid nitrogen at a pressure of  $10^5$  Pa. The peak-to-valley thermal slope error *versus* peak temperature  $T_{\text{peak}}$  of the crystal,  $\theta(T)$ , should be the average of the term  $\alpha(T - T_f)$  in the volume of the crystal. For example,

$$\theta_{\text{th}}(T) = \overline{|\alpha(T)|(T - T_f)}. \quad (6)$$

As the temperature of the crystal is in the range ( $T_0, T_{\text{peak}}$ ), with  $T_f \leq T_0 < T_{\text{peak}}$ , the average should be made in this temperature

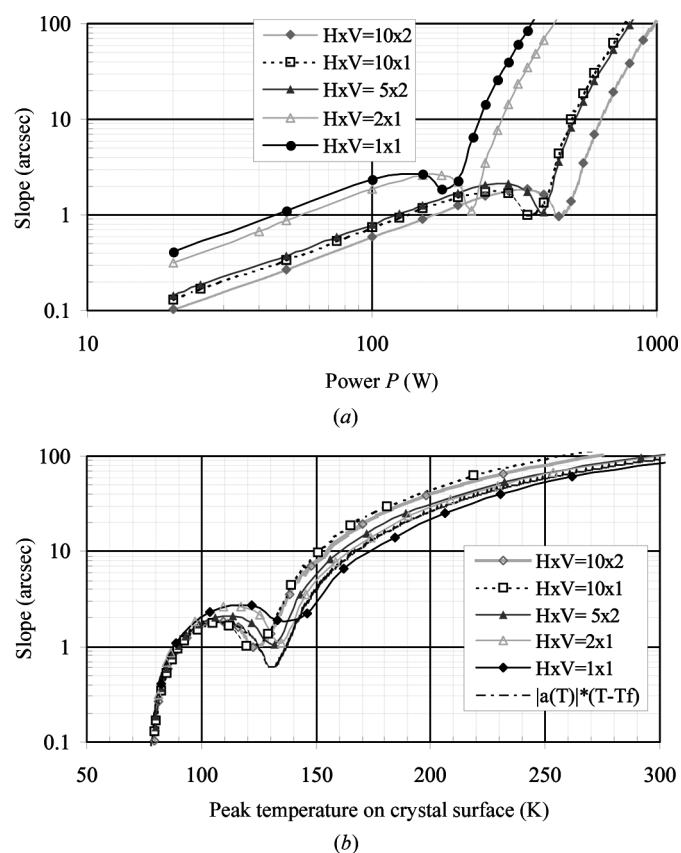


**Figure 6** Thermal slope error *versus* (a) absorbed power and (b) peak temperature on the crystal surface for different beam sizes. The calculations were made with Gaussian distributions, surface absorption and a cooling coefficient  $h_{\text{cv}} = 5000 \text{ W m}^{-2} \text{ K}^{-1}$ .

range. For a value of  $T_0 = 0.75T_{\text{peak}} + 0.25T_f$ , the calculated thermal slope by equation (6) is shown in Fig. 6(b). The result from the simple model given by equation (6) is very close to the shape of the slope–temperature curves. It is clear that the curves shown in Figs. 4(b), 5(b) and 6(b) are the reflection of the thermal expansion coefficient  $\alpha$ . The cooling parameters have slight influences on the relation between the thermal slope error and the peak temperature of the crystal. However, the beam size does have a significant influence on the relationship between the thermal slope error and the peak temperature of the crystal.

#### 4.4. Thermal slope error *versus* position of the footprint

For the channel-cut crystal used on beamline ID09, the position of the footprint on the first crystal is not necessarily centered. When the incident angle (Bragg angle) changes, the position of the footprint on the first crystal moves. The footprint is closer to the downstream end of the first crystal at large Bragg angles. When the Bragg angle is  $2.27^\circ$  the footprint is closer to the upstream end of the first crystal.

To investigate the importance of the footprint position on the crystal, FEA was performed for a centered and off-centered footprint and for two cooling coefficients. The heat load was calculated including Gaussian distributions and surface absorption. The thermal slope error *versus* power is shown in Fig. 7. The change in the slope error for the two positions is negligible in the linear region and about 20% in the non-linear region.

#### 5. Comparison of FEA results with test results

The first set of rocking curves was measured with the U46 undulator at a fixed gap of 15.8 mm. The absorbed power was varied between 20 and 240 W. The storage ring was operated in 16-bunch mode with a maximum electron beam current of 90 mA ([http://www.esrf.fr/machine/operation/machine/modes/operation\\_modes.html](http://www.esrf.fr/machine/operation/machine/modes/operation_modes.html)). The different powers were obtained at different currents and slit openings. After the installation of the in-vacuum undulator U17 in the beamline, a second set of measurements was undertaken with both undulators in tandem. The second undulator allowed us to increase the heat load dramatically without having to change the slit size. Thus, the normal incident beam size was fixed at 10.35 mm (H) × 2.3 mm (V), and the U46 undulator gap was fixed at 16.9 mm, while the U17 undulator was used as a variable heat source. The storage ring was operated in 16-bunch mode. The total power absorbed by the crystal varied from  $P = 254$  to 548 W by changing the gap of the U17

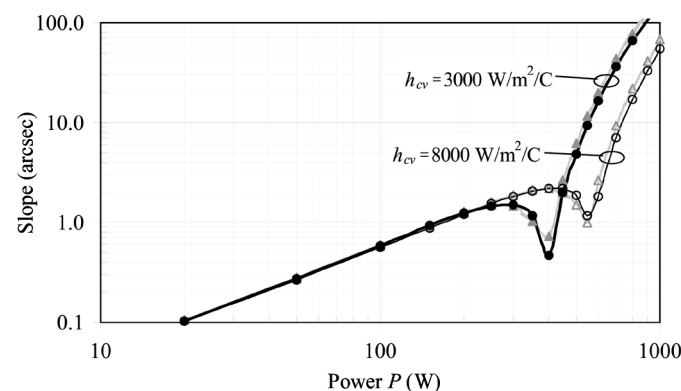


**Figure 7** Thermal slope error *versus* absorbed power for the footprint at the center (continuous line) or at the downstream end (dashed line) on the first crystal surface.

undulator from a fully open position to a minimum gap of 6.5 mm. Rocking curves were measured and the FWHM rocking-curve width was deduced. The measured rocking-curve widths are shown in Fig. 8 and compared with calculated results.

The FEA was performed with a cooling coefficient of  $h_{cv} = 3000 \text{ W m}^{-2} \text{ C}^{-1}$ , a beam size of 10.35 mm (H)  $\times$  2.3 mm (V), and the heat load was treated with a Gaussian distribution and volume absorption [see equation (4)]. As both undulators were used in the second set of measurements, the power of the two undulators in series was calculated with the *SRW* software including absorption corrections for losses in windows and filters. The effective standard deviations  $\sigma_x$  and  $\sigma_y$  were determined by fitting the power density of the two undulators in series to a Gaussian distribution. When the gap of U46 is 16.9 mm and the gap of U17 is 10.0 mm, we find that  $\sigma_x = 5.58 \text{ mm}$ ,  $\sigma_y = 1.44 \text{ mm}$ . Indeed, the measurements were carried out using a variable gap with the U17 undulator. However, the variation of the beam size with the U17 gap is small. Additionally, the results shown in §4.1 indicate that the influences of these standard deviations on the thermal slope error are not very significant for our beam size. Therefore, fixed values of the standard deviations ( $\sigma_x = 5.58 \text{ mm}$ ,  $\sigma_y = 1.44 \text{ mm}$ ) are a good simplification for the FEA.

From FEA one knows that the slope error is independent of the cooling coefficient  $h_{cv}$  in the linear region. Therefore it is not very important to know the exact value of  $h_{cv}$  (or cooling flow parameters) in the power range 0–250 W. However, the exact value of the cooling coefficient is very important for powers greater than 250 W.

For a perfect Si crystal the rocking-curve width in the zero power limit  $\text{FWHM}_{P=0}$  should be the intrinsic rocking-curve width, which is  $\text{FWHM}_{\text{intr}} = 0.67 \text{ arcsec}$  for Si(333) at 24 keV. However, the value of  $\text{FWHM}_{P=0}$  at  $P_{\text{total}} = 0 \text{ W}$ , deduced by extrapolation (and confirmed by ‘cold beam’ measurements), was  $\text{FWHM}_{P=0} = 1.3 \text{ arcsec}$ , thus larger than  $\text{FWHM}_{\text{intr}} = 0.67 \text{ arcsec}$ . This could be due to mounting/fabrication-induced strain in the monochromator. The slope of the mounting strain  $\theta_0$  can be calculated from

$$\theta_0 = (\text{FWHM}_{P=0}^2 - \text{FWHM}_{\text{intr}}^2)^{1/2} = 1.1 \text{ arcsec}. \quad (7)$$

Let us designate  $\theta_{\text{th}}$  as the pure thermal slope error computed by FEA. The rocking-curve width of the crystal without initial deformation is then determined by

$$\text{FWHM}_{c0} = (\theta_{\text{th}}^2 + \text{FWHM}_{\text{intr}}^2)^{1/2}. \quad (8)$$

When the crystal is not perfect, the initial deformation is superimposed on the thermal deformation induced by the X-ray beam. The

rocking-curve width of the crystal with initial deformation can then be estimated by

$$\text{FWHM}_c = [(\theta_{\text{th}} + \theta_0)^2 + \text{FWHM}_{\text{intr}}^2]^{1/2}. \quad (9)$$

The rocking-curve width calculated using (7) is shown in Fig. 8 as well as the maximum temperature of the crystal. A FEA calculation was also performed for a beam size of 5.18 mm (H)  $\times$  1.15 mm (V) (half the 10.35 mm  $\times$  2.3 mm beam size in the other calculations) in the power range 0–200 W. This was done to accommodate the first set of measurements which were carried out with beams varying from 1.2 mm  $\times$  1.2 mm to 10.35 mm  $\times$  2.3 mm. Initially the thermal slope error  $\theta_{\text{th}}$  was computed using several values of cooling coefficient  $h_{cv}$ . Comparison between the calculated rocking-curve width  $\text{FWHM}_c$  (denoted as 10.35  $\times$  2.3, 5.18  $\times$  1.15 in Fig. 8) and the measured rocking-curve width  $\text{FWHM}_{\text{test}}$  (denoted as test-1 and test-2 in Fig. 8) suggests that the effective cooling coefficient is  $h_{cv} = 3000 \text{ W m}^{-2} \text{ K}^{-1}$ . The measurements confirmed the FEA prediction of a minimum slope error near 125 K and the three regions in the slope–power curves. The calculated maximum temperature of the crystal is about 125 K at the minimum of the FWHM–power curve (around  $P = 420 \text{ W}$ ). At this temperature the thermal expansion coefficient of the Si crystal approaches zero. Only at the warmest point, *i.e.* the center of the footprint, is the temperature 125 K; elsewhere it is lower. Therefore the thermal deformation is not zero but at its minimum. The excellent agreement between the measurements and FEA results confirms the validity of the finite-element modeling. Note that the FEA was made with a fixed beam size of 10.35 mm (H)  $\times$  2.3 mm (V), and results in §4.3 indicate that the thermal slope error could be slightly higher with a smaller beam size (but same total power). The first set of measurements were carried out with a beam size varying up to 10.35 mm (H)  $\times$  2.3 mm (V) and for a power lower than 240 W. This can explain why the test results (test-1) in the range 0–240 W are slightly larger than the calculated results (10.35  $\times$  2.3), and slightly smaller than the calculated results with beam size 5.18 mm (H)  $\times$  1.15 mm (V) as shown in Fig. 8.

It should be noted that the shape of the curve in Fig. 8 is similar to results reported by Lee *et al.* (2001). However, in that paper the rocking-curve-width minimum occurred at 130 W. This new study clearly suggests that the thermal contact of that crystal was not optimal. This might be linked to the fact that for their crystal there was no detectable strain, whereas in our work the crystal is strained by 1.1 arcsec, which results in superior thermal contact. Furthermore, it should be noted that, although the power involved in this study is comparable, our power densities are several times smaller than those reported by Lee *et al.* (2000, 2001).

## 6. Summary

The thermal deformation of the channel-cut Si monochromator in ID09, which is indirectly cooled by liquid nitrogen, was studied experimentally and by finite-element analysis. The rocking-curve width (FWHM) was measured and calculated for heat loads between 20 and 570 W. Excellent agreement between the experimental measurements and theoretical results was observed. The measurements confirm the FEA prediction of a local minimum in the slope error when the power is raised to the point where the maximum temperature in the footprint reaches 125 K. At this temperature the ratio between the thermal expansion and the thermal conductivity is zero, which is the best high-power working point for the monochromator. More generally the FEA analysis has identified three power regions:

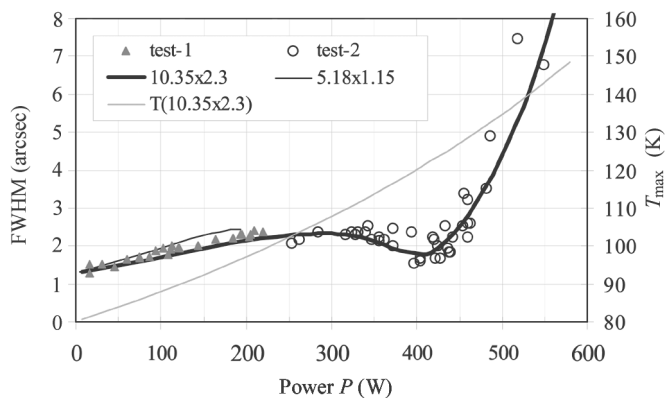


**Figure 8** Rocking-curve width FWHM and maximum temperature on the channel-cut Si crystal *versus* total absorbed power. 10.35  $\times$  2.3 and 5.18  $\times$  1.15 denote calculated results with corresponding beam sizes.

(i) *The linear region.* In this region the thermal slope error is linearly proportional to the absorbed power. The temperature of the crystal is less than 125 K. The thermal slope error is independent of the value of the cooling coefficient ( $h_{cv} \geq 3000 \text{ W m}^{-2} \text{ K}^{-1}$ ).

(ii) *The transition region.* The temperature of the crystal is close to 125 K, the thermal slope error decreases below the extrapolated line from the linear region. The value of the slope error in this region depends on the cooling coefficient and the footprint (or slit opening).

(iii) *The non-linear region.* The temperature of the crystal is higher than 125 K, the thermal slope error increases faster than linear. The cooling coefficient and the footprint are of great importance for the value of the slope error. The efficiency of the cooling scheme, *i.e.* the value of the cooling coefficient, is of paramount importance. Direct cooling of the silicon crystal is necessary in this high-power range.

The authors are grateful to W. Reichenbach and H. Hanfland for their contributions to this work, and A. Freund and F. Comin for their interest and encouragement. The APS is supported by the US Department of Energy, Office of Basic Energy Sciences, under Contract No. W-31-109-Eng-38. This work was performed while WKL was a visiting scientist at the ESRF.

## References

- Bilderback, D. H., Freund, A. K., Knapp, G. S. & Mills, D. M. (2000). *J. Synchrotron Rad.* **7**, 53–60.
- Chantrenne, P., Marion, Ph., Zhang, L. & Vallet, L. (2003). *J. Heat Transfer*. Submitted
- Chubar, O. & Elleaume, P. (1998). *Proceedings of the European Particle Acceleration Conference*, Stockholm, Sweden, pp. 1177–1179. Bristol: IOP.
- Dejus, R. J. & del Rio, M. S. (1996). *Rev. Sci. Instrum.* **67**(9), CD-ROM.
- Hoszowska, J., Mocella, V., Zhang, L., Migliore, J. S., Freund, A. & Ferrero, C. (2001). *Nucl. Instrum. Methods A* **467/468**, 631–634.
- Lee, W. K., Fernandez, P. & Mills, D. (2000). *J. Synchrotron Rad.* **7**, 12–17.
- Lee, W. K., Fezzaa, K., Fernandez, P., Tajiri, G. & Mills, D. M. (2001). *J. Synchrotron Rad.* **8**, 22–25.
- Lee, W. K., Mills, D. M., Assoufid, L., Blasdel, R. C., Fernandez, P., Rogers, C. S. & Smither, R. K. (1995). *Opt. Eng.* **34**, 418–425.
- Marot, G. (1995). *Opt. Eng.* **34**, 426–431.
- Marot, G. & Rossat, M. (1992). *Proc. SPIE*, **1739**, 464–473.
- Marot, G., Rossat, M., Freund, A., Joksche, S., Kawata, H., Zhang, L., Ziegler, E., Berman, L., Chapman, D., Hastings, J. B. & Iarocci, M. (1992). *Rev. Sci. Instrum.* **63**(1), 477–480.
- Mocella, V., Ferrero, C., Freund, A., Hoszowska, J., Zhang, L. & Epelboin, Y. (2001). *Nucl. Instrum. Methods A* **467/468**, 414–417.
- Mocella, V., Lee, W. K., Tajiri, G., Mills, D., Ferraro, C. & Epelboin, Y. (2003). *J. Appl. Cryst.* **36**, 129–136.
- Rogers, C. S., Mills, D. M., Lee, W. K., Knapp, G. S., Holmberg, J., Freund, A., Wulff, M., Rossat, M., Hanfland, M. & Yamaoka, H. (1995). *Rev. Sci. Instrum.* **66**(6), 2494–2499.
- Schotte, F., Techert, S., Anfinrud, P. A., Srajer, V., Moffat, K. & Wulff, M. (2002). *Third-Generation Hard X-ray Synchrotron Radiation Sources*, edited by Dennis Mills, pp. 345–401. New York: John Wiley & Sons.
- Tajiri, G., Lee, W. K., Fernandez, P., Mills, D. M., Assoufid, L. & Amirouche, F. (2001). *J. Synchrotron Rad.* **8**, 1140–1148.
- Takagi, S. (1962). *Acta Cryst.* **15**, 1311–1312.
- Takagi, S. (1969). *J. Phys. Soc. Jpn.* **26**, 1239.
- Taupin, D. (1964). *Bull. Soc. Fr. Minér. Crist.* **87**, 69.
- Taupin, D. (1967). *Acta Cryst.* **23**, 25–35.
- Zhang, L. (1993). *Proc. SPIE*, **1997**, 223–235.
- Zhang, L. (1999). ESRF Internal Report ID9xtal99. ESRF, BP 220, 38043 Grenoble CEDEX, France.
- Zhang, L., Hoszowska, J., Migliore, J. S., Mocella, V., Ferrero, C. & Freund, A. (2001). *Nucl. Instrum. Methods A* **467/468**, 409–413.